TECHNISCHE MECHANIK
European Journal of Engineering Mechanics
Diamond Open Access
journal homepage: www.ovgu.de/techmech

Tech. Mech., Vol. 46, Is. 1, (2026), 126–135
Received: 01.11.2025
Accepted: 14.01.2026
Available online: 16.02.2026

Definition and computation of a flutter safety margin for quadcopters by chained 2-DOF aeroelastic models

Dávid András Horváth[1]*, János Lelkes[2], Balázs Farkas[1], Tamás Kalmár-Nagy[1]

[1] Department of Fluid Mechanics, Faculty of Mechanical Engineering, Budapest University of Technology and Economics
Bertalan Lajos u. 4 - 6, H-1111 Budapest, Hungary.
[2] Robert Bosch Kft.

Abstract: When thin, flexible structures, such as the rotors of a quadcopter, are subjected to airflow, aeroelastic phenomena (e.g. flutter) may occur due to the interaction of elastic, inertial, and aerodynamic forces. We examine rotor blade flutter during forward flight. In this regime, the relative wind experienced by the rotor blades changes periodically, which may result in parametric excitation and a corresponding reduced critical velocity. To capture the variation of relative wind along the rotor radius, we construct a three-dimensional reduced-order model by chaining multiple two-degree-of-freedom aeroelastic models. The aerodynamic forces are computed using a quasi-steady approach. Wind tunnel measurements on the quadcopter are used to obtain the rotor angular velocities corresponding to different forward flight speeds. We then compute the stability chart for the quadcopter by numerically solving the equations of motion of the reduced-order model. From this chart we can determine -for a given rotor speed and forward flight velocity- the minimal speed increase (the flutter safety margin) required for the rotors to lose their stability.

Keywords: aeroelasticity, fluid-structure interaction, numerical stability analysis, parametric excitation, quadcopter

1 Introduction

Aeroelastic phenomena affect several types of slender elastic structures subjected to airflow, such as flexible wings, helicopter rotor blades, and wind turbines. Aeroelasticity studies the interactions between inertial, elastic, and aerodynamic forces on flexible structures that are exposed to airflow. The theory of aeroelasticity is extensively covered in the literature Bisplinghoff et al. (2013); Dowell (2022); Fung (2008). One dangerous aeroelastic instability is called flutter, which is a dynamic stability loss Dowell (2022). A famous example of flutter is the vibrations and structural failure of the Tacoma Narrows bridge Harish (2018); Tac (2020).
Airflow oscillations can cause parametric excitation in aeroelastic systems Meshki et al. (2020). In parametric excitation the source of excitation is the time-varying modification of a system parameter. In the case of airflow oscillations, the parameters of the aerodynamic lift and moment are time-varying. The interaction of self- and parametric excitation usually influences the critical wind velocity.
Typically, a two-degrees-of-freedom (2-DOF) reduced-order model is used to investigate flutter and compute the critical velocity Lelkes et al. (2023). However, one major disadvantage of this approach is that it assumes a uniform velocity along the wing, while rotorcraft, such as drones, have a linear velocity distribution along the span of their wings. Thus, it is important to study a more complex reduced-order model to gain a better understanding of flutter safety for these aircraft.
This work investigates a three-dimensional reduced-order model subjected to periodically varying airflow to study flutter in flying drones. In Section 2, we introduce the mathematical model. In Section 3, we compute the stability charts. In Section 4, we introduce the flutter safety margin and compute it during the flight of the drone. In Section 5, we summarize the results.

2 Mathematical model

In this section, we will describe the three-dimensional reduced-order aeroelastic model. The building block of this model is a two-degrees-of-freedom (2-DOF) aeroelastic model shown in Fig. 1. The two degrees of freedom in the model are the pitching (α) and plunging (h) degrees of freedom. In this model, we assume that the center of gravity (denoted by G) is located in the middle of the wing. We denote the semichord by b and compute the distance between the elastic axis and the center of gravity by $a \cdot b$. The equations of motion of this model are Abdelkefi et al. (2013).

$$\begin{aligned} m\ddot{h} + c_h\dot{h} + k_h h &= -L, \\ I_\alpha\ddot{\alpha} + c_\alpha\dot{\alpha} + k_\alpha\alpha &= M, \end{aligned} \tag{1}$$

where h and α describe the vertical (plunge) displacement (positive downwards) and angular (pitch) displacement (positive in the clockwise direction), respectively. The mass of the wing is m and I_α is the moment of inertia. The stiffness and damping coefficients for the plunge DOF are denoted by k_h and c_h, respectively. For the pitch DOF, these coefficients are denoted by k_α and c_α. L and M denote the aerodynamic lift and moment (together they will be called the aerodynamic forces). To compute the

* E-mail address: horvathd1@edu.bme.hu
doi: 10.24352/UB.OVGU-2026-013

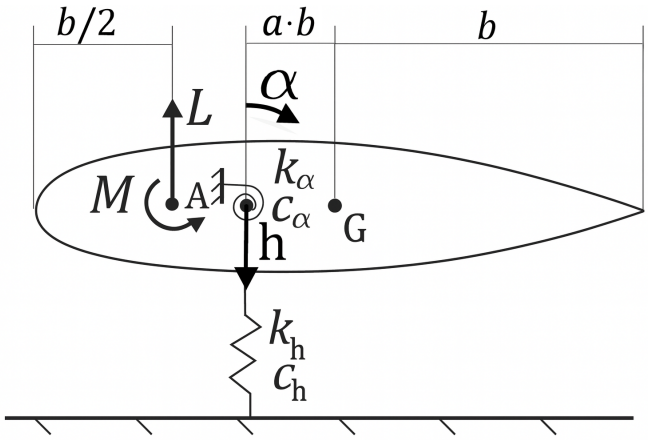

Fig. 1: The 2-DOF aeroelastic model.

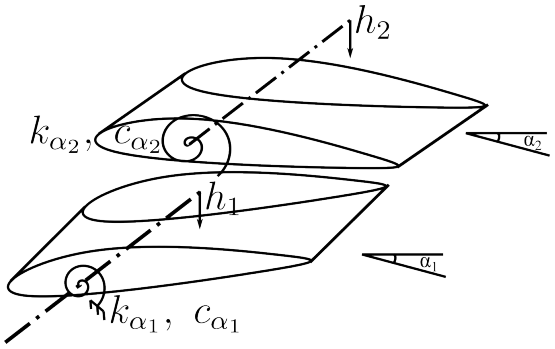

Fig. 2: The three-dimensional reduced order model.

aerodynamic forces L and M, we apply the quasi-steady approximation of the Theodorsen lift function Theodorsen (1935). Thus,

$$\begin{aligned} L &= 2\pi\rho U^2 bS\left[\alpha + \frac{\dot{h}}{V} + b\left(\frac{1}{2} - a\right)\frac{\dot{\alpha}}{V}\right], \\ M &= 2\pi\rho U^2 b^2 S\left(a + \frac{1}{2}\right)\left[\alpha + \frac{\dot{h}}{V} + b\left(\frac{1}{2} - a\right)\frac{\dot{\alpha}}{V}\right], \end{aligned} \tag{2}$$

where S is the span of the wing, a is defined via Fig. 1, ρ is the density of the air and V is the velocity of the air. One big disadvantage of this model is that it assumes a constant velocity distribution along the span of the wing. This assumption is not valid for rotorcraft, since in their case the velocity increases linearly from the hub to the tip of the wing.
We eliminate this disadvantage by dividing the wing into mulitple segments. To model the bending of the wing each segment is treated as an Euler-Bernoulli beam element. In addition the segments are connected to each other through torsional springs. The construction is shown in Fig. 2 for two wing segments, but can be easily generalized for more segments. We denote by h_i, α_i the average vertical and pitching displacement of the i-th wing segment, respectively. These average displacements will be used to compute the aerodynamical forces. The equation of motion for this three-dimensional model is

$$\mathbf{M}\ddot{\mathbf{x}} + \mathbf{C}\dot{\mathbf{x}} + \mathbf{K}\mathbf{x} = \begin{bmatrix} L_{1,3}\left(\ddot{h}_1, \dot{h}_1, \alpha_1, \dot{\alpha}_1, \ddot{\alpha}_1\right) + L_{2,1}\left(\ddot{h}_2, \dot{h}_2, \alpha_2, \dot{\alpha}_2, \ddot{\alpha}_2\right) \\ L_{1,4}\left(\ddot{h}_1, \dot{h}_1, \alpha_1, \dot{\alpha}_1, \ddot{\alpha}_1\right) + L_{2,2}\left(\ddot{h}_2, \dot{h}_2, \alpha_2, \dot{\alpha}_2, \ddot{\alpha}_2\right) \\ L_{2,3}\left(\ddot{h}_2, \dot{h}_2, \alpha_2, \dot{\alpha}_2, \ddot{\alpha}_2\right) \\ L_{2,4}\left(\ddot{h}_2, \dot{h}_2, \alpha_2, \dot{\alpha}_2, \ddot{\alpha}_2\right) \\ M_1\left(\ddot{h}_1, \dot{h}_1, \alpha_1, \dot{\alpha}_1, \ddot{\alpha}_1\right) \\ M_2\left(\ddot{h}_2, \dot{h}_2, \alpha_2, \dot{\alpha}_2, \ddot{\alpha}_2\right) \end{bmatrix}, \tag{3}$$

where $\mathbf{M}$, $\mathbf{C}$, and $\mathbf{K}$ are the mass, damping, and stiffness matrices respectively. The state vector $\mathbf{x} = [x_1, x_2, x_3, x_4, x_5, x_6]^T$ has six variables: the two plunging displacements $h_1,\ h_2$, the two spanwise rotational displacements (these are necessary only for the Euler-Bernoulli model) θ_1, θ_2 and the two pitching displacements $\alpha_1,\ \alpha_2$, i.e., $x_1 = h_1, x_2 = h_2, x_3 = \theta_1, x_4 = \theta_2,\ x_5 = \alpha_1,\ x_6 = \alpha_2$. $M_i\left(\ddot{h}_i, \dot{h}_i, \alpha_i, \dot{\alpha}_i, \ddot{\alpha}_i\right)$ is the moment acting on the i-th wing segment and $L_{i,j}\left(\ddot{h}_i, \dot{h}_i, \alpha_i, \dot{\alpha}_i, \ddot{\alpha}_i\right)$ denotes the load on the j-th node of the i-th wing segment due to the lift force. These loads were computed assuming a uniform force distribution across each wing element according to

$$L_{i,1} = \frac{L_i \frac{S}{n}}{2}, \quad L_{i,2} = \frac{L_i \frac{S^2}{n^2}}{12}, \quad L_{i,3} = \frac{L_i \frac{S}{n}}{2}, \quad L_{i,4} = -\frac{L_i \frac{S^2}{n^2}}{16}. \tag{4}$$

Tab. 1: Numerical values of the parameters in the three-dimensional reduced order model.

Parameter name	Parameter value
a	0
b	0.017 m
c_h	0.003 kg/s
c_α	0.006 kg m^2/s
Θ	0.00023 kg m^2
k_h	250 N/m
k_α	0.49 N m/rad
m	0.008 kg
S	0.167 m
ρ	1.2 kg/m^3

The simplified mass and stiffness matrices are given (for 2 segments) by

$$\mathbf{M} = \begin{pmatrix} \frac{13m}{35} & 0 & \frac{9m}{140} & -\frac{13mS}{1680} & 0 & 0 \\ 0 & \frac{mS^2}{420} & \frac{13mS}{1680} & -\frac{mS^2}{1120} & 0 & 0 \\ \frac{9m}{140} & \frac{13mS}{1680} & \frac{13m}{70} & -\frac{1}{840}(11mS) & 0 & 0 \\ -\frac{13mS}{1680} & -\frac{mS^2}{1120} & -\frac{1}{840}(11mS) & \frac{mS^2}{840} & 0 & 0 \\ 0 & 0 & 0 & 0 & \mathrm{k}\alpha & 0 \\ 0 & 0 & 0 & 0 & 0 & \mathrm{k}\alpha \end{pmatrix}, \tag{5}$$

$$\mathbf{K} = \begin{pmatrix} 64k_h & 0 & -32k_h & 8k_hS & 0 & 0 \\ 0 & \frac{16k_hS^2}{3} & -8k_hS & \frac{4k_hS^2}{3} & 0 & 0 \\ -32k_h & -8k_hS & 32k_h & -8k_hS & 0 & 0 \\ 8k_hS & \frac{4k_hS^2}{3} & -8k_hS & \frac{8k_hS^2}{3} & 0 & 0 \\ 0 & 0 & 0 & 0 & 2k_\alpha & -k_\alpha \\ 0 & 0 & 0 & 0 & -k_\alpha & k_\alpha \end{pmatrix}, \tag{6}$$

where m, S, k_h, k_α are the mass, span of the wing and the stiffness coefficients of the 2-DoF model, respectively. We assume proportional damping, meaning that the damping matrix $\mathbf{C}$ is a multiple of the stiffness matrix $\mathbf{K}$, i.e.,

$$\mathbf{C} = d\mathbf{K}, \tag{7}$$

where d is the damping coefficient. We computed d such that the critical velocity for one wing segment is the same as the critical velocity of the 2-DoF model.

Note that our model does not take into account the centrifugal forces acting on the rotor blade. These forces have a stiffening effect resulting in an increased flutter velocity. Thus our results might be regarded as a conservative estimate for the flutter velocity.

For the model we have taken the structural parameters from the work of Abdelkefi et al. (2013) but scaled them to match the dimensions and mass of our drone's propeller. The resulting parameters are shown in Tab. 1. We will now compute the critical velocity of the model, which is the flow velocity at which the system loses its stability and flutter oscillations occur. We assume a linear velocity distribution along the wing given by

$$v_i = v\frac{i}{n}, \tag{8}$$

where v_i is the wind velocity at the i-th wing segment. To compute the critical velocity, we determine the eigenvalues of the system's Jacobian for wind velocities starting from 0, increasing by 1 m/s up to 100 m/s. As the velocity increases, a pair of complex conjugate eigenvalues will cross the imaginary axis. The velocity at which this occurs is the critical velocity, which is shown in Fig. 3 as a function of the number of wing segments.

The critical velocity of the two-degrees-of-freedom (2-DOF) model is 52 m/s. The 3-dimensional model with 1 wing segment results in the same critical velocity. As the number of wing segments increases, the critical velocity also increases to 70 m/s. Thus, the use of the three-dimensional model results in 35 – 40% higher critical velocity. Since increasing the number of segments beyond $n > 6$ does not change the critical velocity, we will use $n = 6$ throughout the rest of this paper.

We note that the critical velocity changes proportionally to the damping coefficient d (see Eq. (7)). This means that a 10% uncertainty in d causes a 10% uncertainty in the flutter velocity. In the present manuscript we will focus on investigating the structure of the stability boundary under parametric excitation.

3 Stability charts

In this section, we will compute stability charts for the three-dimensional model, which show as a function of the rotor speed and the forward flight velocity, whether flutter occurs, i.e., the stability of the system.

As a first step, we need to compute the time-varying relative wind velocity experienced by the rotor blade as a function of the rotor speed and the forward flight velocity. This velocity is time-varying, because as the rotor blade travels forward (in the same

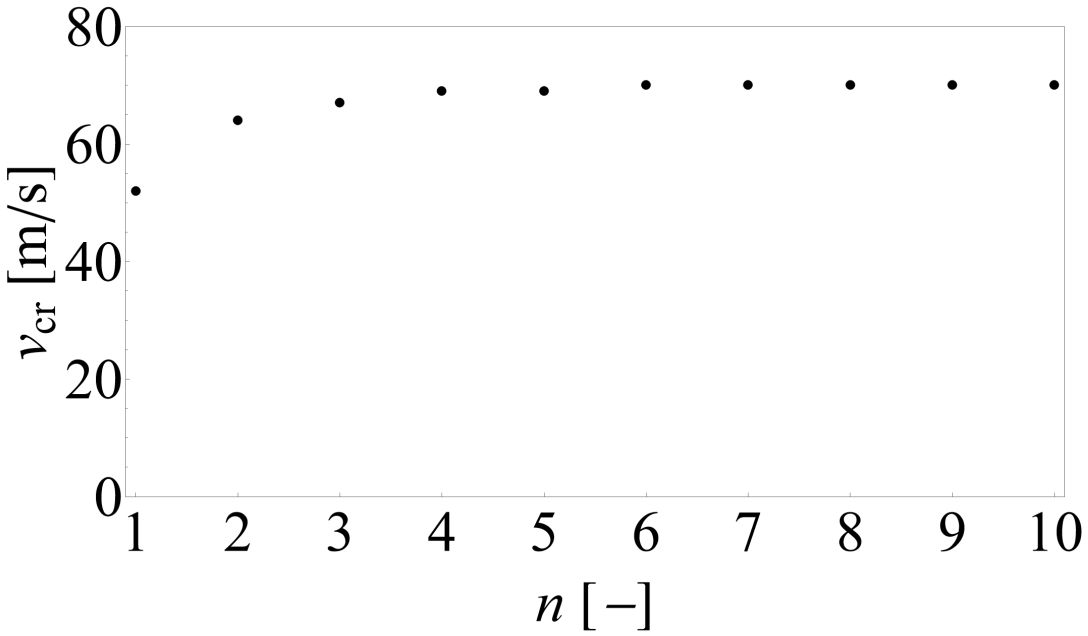

Fig. 3: Comparison of the critical velocity when using Euler-Bernoulli beam segments.

direction as the rotorcraft is flying), the relative velocity due to the flight of the drone is subtracted from the relative velocity due to the rotor rotation. As the blade travels backward (in the opposite direction to the rotorcraft flight), the opposite happens and the relative velocity increases. The relative velocity can thus be written as

$$v(t, s) = v_r + v_f \sin(\omega t), \tag{9}$$

where ω is the angular velocity of the rotor, v_f is the forward velocity of the drone, and

$$v_r = \omega \cdot s, \tag{10}$$

is the rotational velocity of the wing tip with s being the distance from the hub of the rotor.

First, we computed the stability chart of the 2-DoF model by carrying out numerical simulation of Eq. (1) using Wolfram Mathematica with the built-in stiffness switching method, which detects the stiffness of the differential equation based on which it switches between an explicit and an implicit solver. We applied the initial condition $\alpha_1(0) = 0.1$. We ran the simulations for 100 s and considered the system unstable if the tip rotation $\alpha_n(t)$ exceeded 0.1 at any point during the simulation.

Unfortunately such an approach was infeasible for the 3-dimensional model due to computational cost. To overcome this problem we have applied Floquet theory and computed the monodromy matrix of the equations of motion. Denoting the monodromy matrix by $\mathbf{\Phi}(t)$, then

$$\mathbf{\Phi}'(t) = \mathbf{A}(t)\mathbf{\Phi}(t), \quad \mathbf{\Phi}(0) = \mathbf{I}, \tag{11}$$

where $\mathbf{A}(t) = \mathbf{A}(t+T)$ ($T = \frac{2\pi}{\omega}$ is the period) is obtained by rewriting the equations of motion as a 1st-order system. The system is stable if every eigenvalue of $\mathbf{\Phi}(T)$ has modulus lower than 1. To compute $\mathbf{\Phi}(T)$ we applied the first-order Magnus expansion (see e.g., the work of (Tal-Ezer et al., 1992)) with 1000 time steps. Thus,

$$\mathbf{\Phi}(T) = e^{\Delta t \mathbf{A}\left(\frac{1}{2}\Delta t\right)} \cdot e^{\Delta t \mathbf{A}\left(1+\frac{1}{2}\Delta t\right)} \cdot \ldots \cdot e^{\Delta t \mathbf{A}\left(T-\frac{1}{2}\Delta t\right)}, \tag{12}$$

where $\Delta t = \frac{T}{1000}$ denotes the timestep size. The stability charts for the 2-DoF model and the 3-dimensional model are shown in Fig. 4, 5. The blue region indicates the unstable region, while the yellow region indicates the stable region. For the 3-dimensional model we plotted the stability chart only for ranges of velocity values, which are realistically achievable during flight due to the large computational effort required by the 3-dimensional model. As shown in the previous section, the 2-DoF model predicts a lower critical velocity compared to the 3-dimensional model. The 3-dimensional model also predicts that as the forward velocity v_f increases, parametric resonance occurs at $v_r = 60$ m/s, which results in a loss of stability at forward flight velocities as low as 6 m/s. This part of the unstable region is realistically achievable during flight. The 2-DoF model however does not predict parametric resonance at this rotor tip velocity, since it predicts a stability loss at a lower $v_r = 52$ m/s. Although it does predict a slight parametric resonance at $v_r = 30$ m/s, for instability $v_f > 40$ m/s is required, which cannot be achieved during normal flight. Another difference in the two stability charts is that the critical velocity decreases as the forward flight velocity increases for the 2-DoF model, but this tendency is reversed for the 3-dimensional model. This means that according to the 3-dimensional model, the rotors are able to spin faster and thus provide more thrust during forward flight.

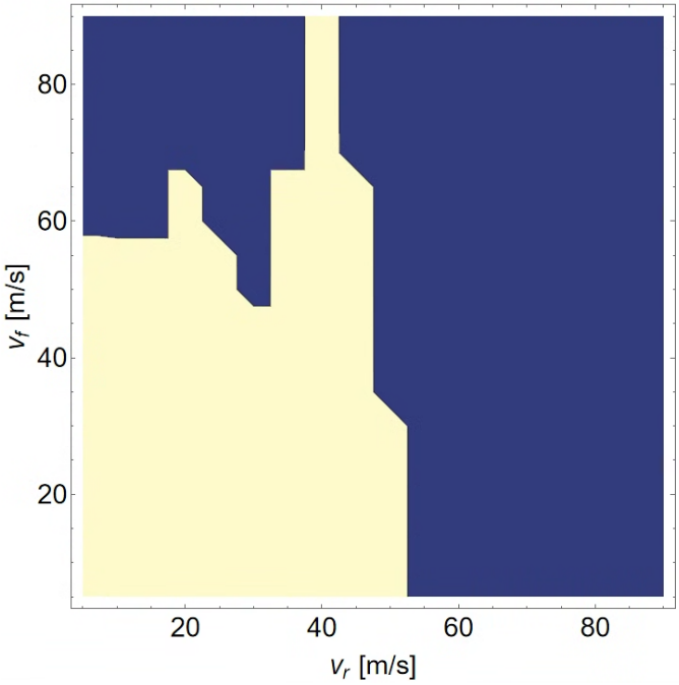

Fig. 4: Stability chart for 2-DoF model.

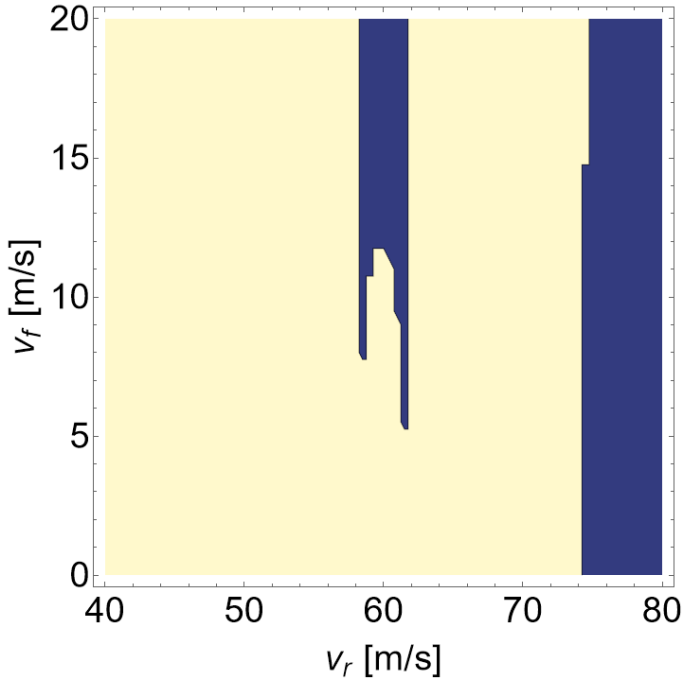

Fig. 5: Stability chart for the 3-dimensional model.

Tab. 2: The velocity of the drone rotor at different forward flight velocities

v [m/s]	f [1/min]
0	3205
2	3206
4	3286
6	3503

Tab. 3: The flutter safety margin during forward flight

v [m/s]	f [1/min]	$\mathcal{S}$ [m/s]
0	3205	7.03
2	3206	5.77
4	3286	3.67
6	3503	0

4 Flutter safety margin

In this section, we define the flutter safety margin and compute it during a flight of the drone. The flutter safety margin is defined as the minimal increase in the relative wind velocity at the tip of the wing which would result in flutter oscillations. This is defined mathematically as the distance between the point (v_f, v_r) and the stability boundary, i.e.,

$$S(v_f, v_r) = \text{dist}((v_f, v_r), B), \tag{13}$$

where S is the flutter safety margin, v_f is the forward velocity of the drone, v_r is the rotational velocity of the wing tip, and B is the stability boundary in the (v_f, v_r) plane. Physically, this flutter safety margin means how much the drone could accelarate until flutter occurs. Another interpretation would be how large a wind gust would need to be for flutter to occur.

To compute the flutter safety margin during the flight of the drone, we first measured the rotor speed corresponding to different forward flight velocities. The goal of the measurement was to determine the working range of a general drone propeller, not to validate the model. The measurements were carried out in the Theodore von Karman low speed wind tunnel of the BME Department of Fluid Mechanics (Hincz et al., 2025). The drone was mounted on a 3 DoF balance inside the wind tunnel. The schematic of the balance system and the quadcopter within the wind tunnel is presented in Fig. 6. The wind velocity was measured by a Prandtl tube from which the pressure signals was converted by a Setra 239 pressure transducer with 0–1389 Pa pressure range and 2% accuracy on the full range. The drag (F_{D1} and F_{D2}) and lift (F_{L1}) forces were acquired by HBM-U9C force transducers with 0.2 accuracy class. The two transducers applied for measuring F_{D1} and F_{D2} were rated to 10 kg and the lift force was measured by a 20 kg rated transducer. The rotation speed of the propellers were extracted from the logged flight controller data after the wind tunnel measurements were completed and the results were monitored by a digitally controlled stroboscope. The main error in the rpm measurement was due to the drain of the battery. This error is larger for higher forward flight velocities, since the current draw is higher in these cases. The forces acting on the drone were measured at different angle of attack, rotor rpm and wind velocity cases. Based on the results the parameters of the equilibrium states, where the forces acting on the drone are in balance (e.g. when the weight force is compensated by the generated lift and the drag is compensated by trust, which corresponds constant speed level flight) were defined by interpolation. The result of the measurement is shown in Fig. 7 and in Tab. 2, where f denotes the rotational velocity of the propeller in revolutions per minute. As the forward velocity of the drone increases, the rotor velocity also increases, which becomes more apparent at higher forward velocities. Note that these rotor velocities result in a rotor tip velocity above the critical velocity for the two-dimensional reduced-order model (which is 52 m/s). Thus, this measurement confirms that the three-dimensional reduced-order model is indeed more accurate than the two-dimensional one.

We show the drone's forward flight velocities and the corresponding rotor tip velocities on the stability chart in Fig. 8 with a black line. This black line is the same as the dotted red line on Figure 7. During forward flight with 6 m/s, the drone crosses slightly into the unstable region. However during our tests we have not observed flutter, which can be due to the error of the rpm measurement, or due to the structural parameters not being accurate enough. The flutter safety margin is shown in Tab. 3. As the drone accelerates, the flutter safety margin decreases and reaches zero at $v_f = 6$ m/s.

For the smallest and largest forward flight velocities we plotted the the torsional displacement of the wing tip in Fig. 9, 10, respectively. We observe that for the zero forward flight velocity, the initial oscillations slowly decay towards zero. For the $v_f = 6$ m/s case, after around 20 s the wing starts to twist in the negative direction. This results in large static deformations, with little amount of oscillations, thus the aeroelastic instability called divergence occurs due to parametric resonance. This is in contrast to the flutter instability, which occurs for $v_f = 0$ and $v_r > 70$ m/s shown in Fig. 11.

5 Summary

In this paper, we develop a three-dimensional reduced-order model for wing flutter of rotorcraft, where the relative wind velocity along the span of the wing is not constant. This model is built by chaining multiple two-dimensional reduced-order models together using torsional springs and treating each wing segment as an Euler-Bernoulli beam element.

First, we computed the critical velocity (i.e., the smallest velocity at which flutter is present) for the three-dimensional model as a function of the number of wing segments. We found that the use of multiple wing segments results in an increase in the critical

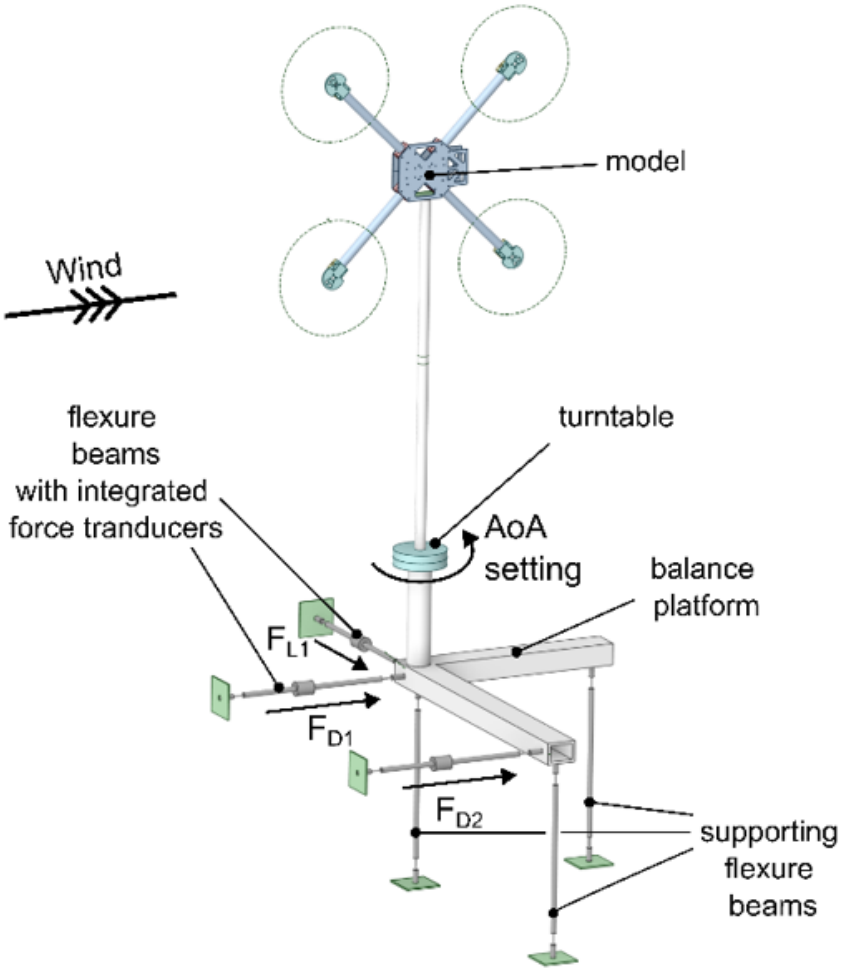

(a) Schematic diagram of the measurement setup.

(b) Picture of the measurement setup.

Fig. 6: The measurement of the drone rotor velocities in the wind tunnel.

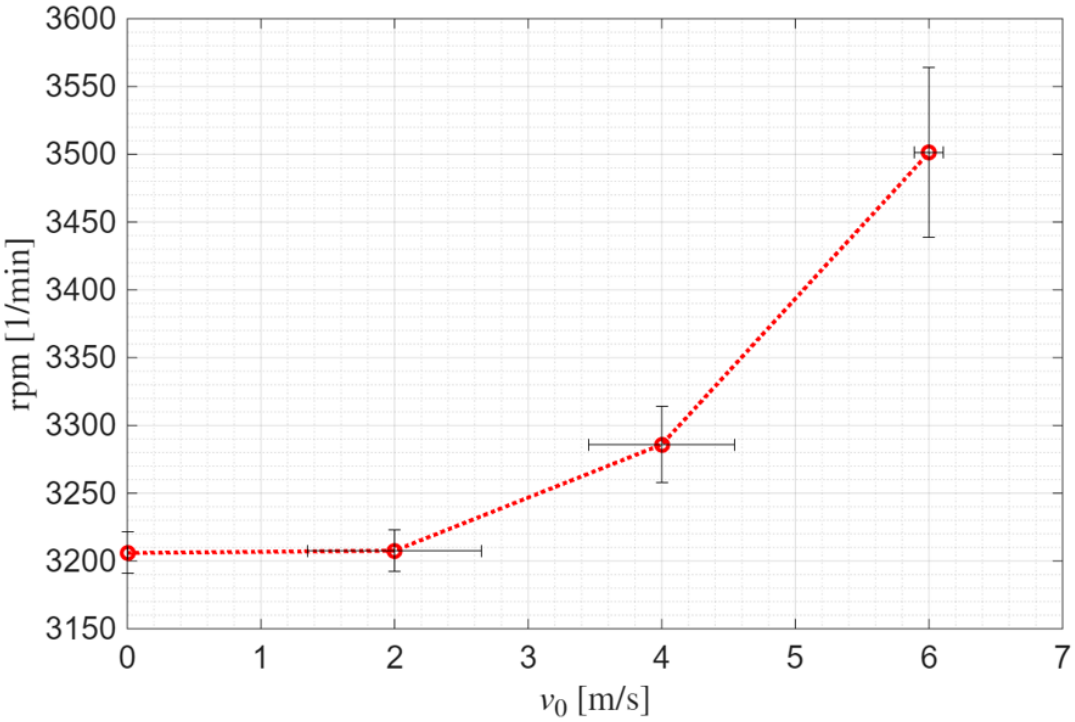

Fig. 7: The rpm of the drone rotor at different forward flight velocities

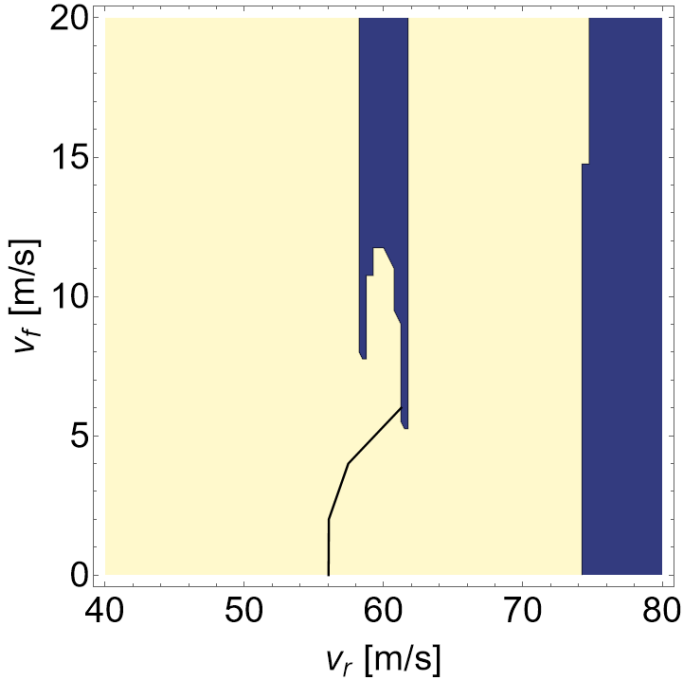

Fig. 8: The rotor tip velocities and their corresponding forward flight velocities shown on the stability chart with a black line.

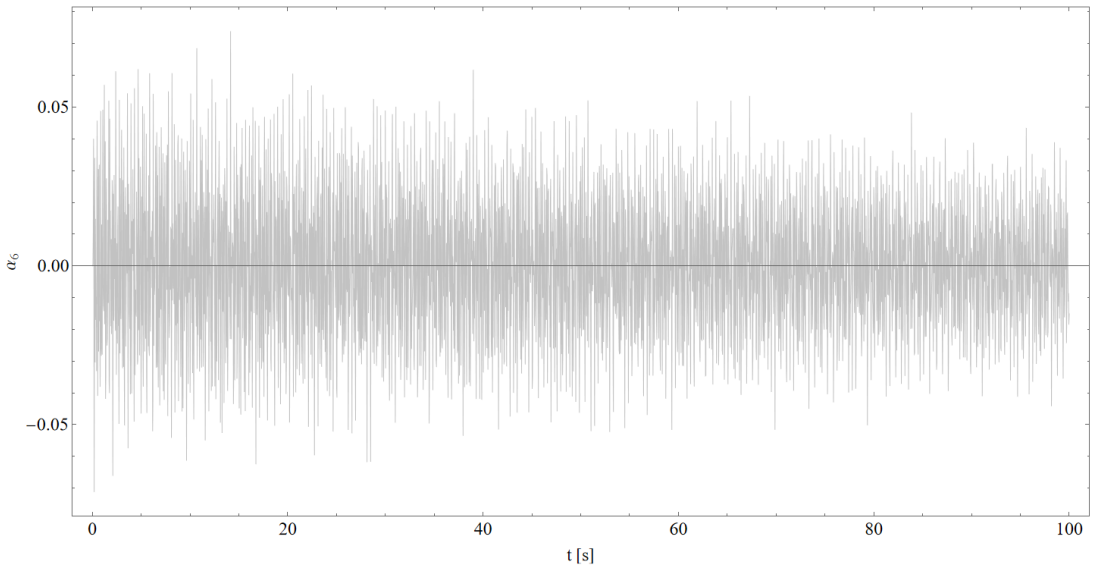

Fig. 9: Time-series chart of the torsional displacement of the wing tip during forward flight with $v_f = 0$ m/s.

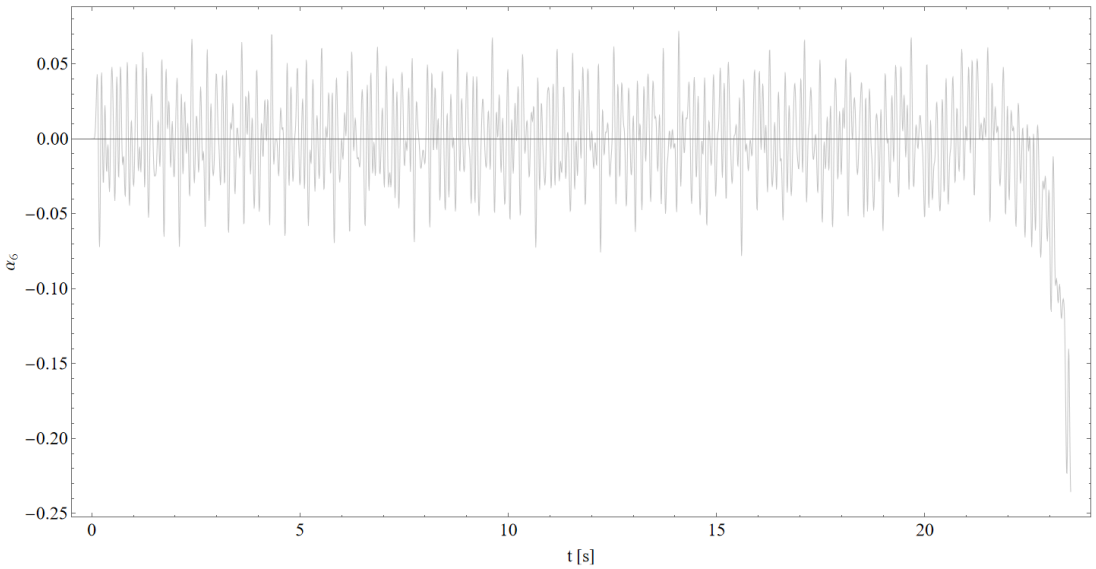

Fig. 10: Time-series chart of the torsional displacement of the wing tip during forward flight with $v_f = 6$ m/s.

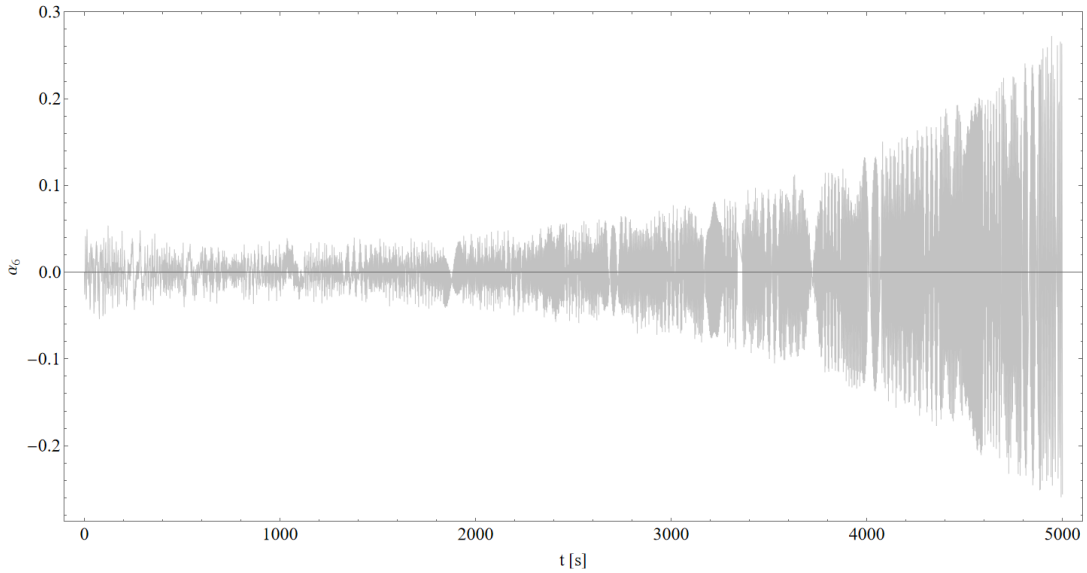

Fig. 11: Time-series chart of the torsional displacement of the wing tip, when the forward velocity of the drone is $v_f = 0$ m/s and the rotor tip velocity $v_r = 80$ m/s.

velocity. As the number of wing segments increases, the critical velocity increases and seems to quickly approach an upper bound. Next, we computed stability charts using the three-dimensional model for various n values and found that increasing the number of wing segments results in the enlargement of the stable region. Based on the stability chart, we defined a flutter safety margin as the distance from the stability boundary. To compute the flutter safety margin during flight, we performed wind tunnel measurements to obtain the rotor tip velocity for different forward flight velocities. Based on the measurement results, we computed the flutter safety margin during forward flight and found that it decreases as the drone accelerates and reaches zero due to parametric resonance. A natural next step for this research would be to accurately measure the structural parameters of the drone rotor and update the stability charts accordingly. Then we could select parameters near the stability boundary and the unstable region and conduct wind tunnel measurements at those rotor speeds and forward flight velocities. This would provide a strong validation of the prediction accuracy of our model.

Acknowledgements

This work has been supported by the Hungarian National Research, Development and Innovation Fund under contract NKFI K137726.
The research reported in this paper is part of project no. TKP-6-6/PALY-2021 has been implemented with the support provided by the Ministry of Culture and Innovation of Hungary from the National Research, Development and Innovation Fund, financed under the TKP2021-NVA funding scheme. The project supported by the Doctoral Excellence Fellowship Programme (DCEP) is funded by the National Research Development and Innovation Fund of the Ministry of Culture and Innovation and the Budapest University of Technology and Economics.

References

Tacoma narrows bridge (1940). https://en.wikipedia.org/wiki/Tacoma_Narrows_Bridge_(1940), 2020.

Abdessattar Abdelkefi, Rui Vasconcellos, Ali H Nayfeh, and Muhammad R Hajj. An analytical and experimental investigation into limit-cycle oscillations of an aeroelastic system. *Nonlinear Dynamics*, 71(1-2):159–173, 2013.

Raymond L Bisplinghoff, Holt Ashley, and Robert L Halfman. *Aeroelasticity*. Courier Corporation, 2013.

Earl H Dowell. *A Modern Course in Aeroelasticity*. Springer, 2022.

Yuan Cheng Fung. *An Introduction to the Theory of Aeroelasticity*. Courier Dover Publications, 2008.

Ajay Harish. Why the Tacoma Narrows bridge collapsed: An engineering analysis. https://www.simscale.com/blog/2018/07/tacoma-narrows-bridge-collapse/, 2018.

Krisztián Hincz, Sherly Joanna Pool-Blanco, and Márton Balczó. Wind analysis of a multispan arch-supported tensile membrane structure. *Journal of Wind Engineering and Industrial Aerodynamics*, 265:106181, October 2025. ISSN 0167-6105. doi: 10.1016/j.jweia.2025.106181.

János Lelkes, Dávid András Horváth, Bálint Lendvai, Balázs Farkas, Bendegúz Dezső Bak, and Tamás Kalmár-Nagy. Data-driven aerodynamic models for aeroelastic simulations. *Journal of Sound and Vibration*, 593:117847, 2023.

Mohammad Mehdi Meshki, Ali Salehzadeh Nobari, and Mohammad Homayoune Sadr. A study on nonlinear, parametric aeroelastic energy harvesters under oscillatory airflow. *Journal of Vibration and Control*, pages 1–11, 2020. doi: 10.1177/1077546320974477.

Hillel Tal-Ezer, Ronnie Kosloff, and Charles Cerjan. Low-order polynomial approximation of propagators for the time-dependent Schrödinger equation. *Journal of Computational Physics*, 100(1):179–187, May 1992. ISSN 0021-9991. doi: 10.1016/0021-9991(92)90318-S.

Theodore Theodorsen. General theory of aerodynamic instability and the mechanism of flutter. *NACA Technical Report*, (496), 1935.